Correspondence to:
H. Wang,
he.wang@noaa.gov

Improving Global Barotropic Tides With Sub-Grid Scale Topography

He Wang[1,2,3] , Robert Hallberg[2], Alan J. Wallcraft[4] , Brian K. Arbic[3] , and Eric P. Chassignet[4]

[1]University Corporation for Atmospheric Research, Boulder, CO, USA, [2]Geophyical Fluid Dynamics Laboratory, National Oceanic and Atmospheric Administration, Princeton, NJ, USA, [3]Department of Earth and Environmental Sciences, University of Michigan, Ann Arbor, MI, USA, [4]Florida State University, Tallahassee, FL, USA

Abstract   In recent years, efforts have been made to include tides in both operational ocean models as well as climate and earth system models. The accuracy of the barotropic tides is often limited by the model topography, which is in turn limited by model horizontal resolution. In this work, we explore the reduction of barotropic tidal errors in an ocean general circulation model (Modular Ocean Model version 6; MOM6) using sub-grid scale topography representation. We follow the methodology from Adcroft (2013, https://doi.org/10.1016/j.ocemod.2013.03.002), which utilizes statistics from finer resolution topographic data sets to represent sub-grid scale features with a light computational cost in a structured finite volume formulation. The geometric effect from sub-grid scale topography can be introduced to the model with only a few parameters at each grid cell. The porous barriers, which are implemented at the walls of the grid cells, are used to modify transport between grid cells. Our results show that the globally averaged tidal error in lower-resolution simulations is significantly reduced with the use of porous barriers. We argue this method is a potentially useful tool to improve simulations of tides (and other flows) in low-resolution simulations.

Plain Language Summary   In recent years, significant attention has been given to simulating tides in diverse ocean and climate models, because of the roles of tides in impacting sea levels. In order to better predict future sea level changes, it is therefore essential to improve the accuracy of surface tides simulated in numerical ocean models. One known source of errors that could impact the accuracy of modeled tides stems from the accuracy of ocean topography in the models, which relies on how many grid boxes (i.e., model resolution) are used to represent the complicated seafloor elevations. The model's resolution, however, is often constrained by the efficiency of computations. Our objective in this study is to enhance the portrayal of ocean topography at a given resolution to minimize tidal errors. To achieve this, we employ a technique known as "porous barriers," which uses approximations to mimic the effects of ocean topography that would be omitted in the models, without imposing significant computational burdens. Our findings demonstrate that this technique of porous barriers can substantially reduce tidal errors in our ocean model. We also expect a wider application of this technique to numerous other physical processes within the ocean.

1. Introduction

Tides are one of the most prominent phenomena in the ocean. Tides arise from differences in the lunar and solar gravitational potential across the Earth. The astronomical tidal forcing drives periodic changes in sea surface height (SSH) and periodic tidal currents. There is a growing need for better understanding tidal interactions with other physical and biogeochemical processes in a changing climate with shorelines altered by sea-level rise and coastal development.

With the advancement of computational power, tides have begun to be explicitly included in both operational global ocean models (high horizontal resolution and short time duration) and global climate and earth system models (often run at low horizontal resolution and long time duration) (Arbic, 2022; Arbic et al., 2010; Barton et al., 2022; Müller et al., 2010; Pal et al., 2023; Schiller & Fiedler, 2007; Thomas et al., 2001). For both high- and low-resolution simulations, it is helpful and sometimes even critical to improve the accuracy of the modeled tides. One important source of tidal error arises from the representation of topography.

In the real ocean, tides are affected by ocean topography (as an abbreviation, we use the term "topography" to refer to ocean basin geometry, ocean bathymetry and shoreline configurations) in many ways. About 1/3 of the
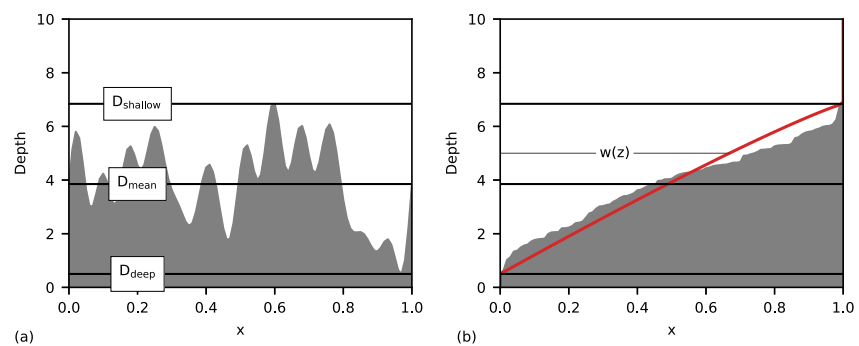
Figure 1. Illustration of the concept of a porous barrier at the facet of a single grid cell. Units of both coordinates in this illustration are arbitrary. At each depth, connectivity, measured by the area of openness, is the same for the realistic sub-grid scale topography in (a) and the sorted topography in (b). The sub-grid scale openness (as a function of depth) is used by the model to constrain transports across grid cells. We can further simplify by using parameters like the maximum, minimum and mean depths to generate an idealized depth profile (red curve in (b)), so that the openness can be solved analytically by the model. $w(z)$ in (b) is a non-dimensional weight function of depth describing the openness of the grid cell, which is used in Equation 5 in Section 3.4.1. The simplified depth profiles are generated following the algorithms in the Appendix of Adcroft (2013).

global tidal dissipation is carried out by the breaking of internal tides in open-ocean regions with rough topography (Egbert & Ray, 2001). In addition to these small scale dissipative processes that often require parameterizations in models, the resonances of global tides are also sensitive to ocean topography. In open oceans, the semi-closed basins guide the propagations of the shallow-water surface gravity waves (Kelvin Waves and Poincaré Waves) forming the amphidromic points and cotidal lines. In the coastal regions, shoreline configuration, shapes of the marginal seas and connectivity of the channels can all influence local tides. The tides of the open ocean are thought to be weakly resonant (Heath, 1981; Wunsch, 1972) due to the fact that there are many global ocean normal modes with frequencies close to those of the astronomical semidiurnal and diurnal tidal forcing (Müller, 2007; Platzman et al., 1981). Some coastal regions (e.g., the Bay of Fundy, English Channel, Hudson Strait, and other locations) are well-shaped for further resonance (Clarke, 1991; Cummins et al., 2010; Garrett, 1972). Previous work has shown that strongly resonant tides in coastal regions have a "back-effect" on tides in the open ocean (Arbic & Garrett, 2010; Arbic et al., 2007, 2009).

Therefore, in order to better simulate tidal resonances in both open oceans, marginal seas and interactions between them, it is crucial to faithfully represent ocean topography in numerical models. However, the accuracy of ocean topography in models is highly restricted by their horizontal resolutions. For discretized model grids, the degrees of freedom of ocean topography is inherently limited by the number of grid cells. This restriction hinders further reduction of tidal errors at a given resolution. Numerical models are unable to resolve sub-grid scale topographic features such as deep ocean channels, ridges and details of shoreline configurations, which leads to misrepresentations of ocean basin and shoreline geometry and resonances of tides and contributes to higher tidal errors in lower resolution simulations (e.g., Egbert et al., 2004). While parameterizations can be used to partially characterize unresolved physical processes such as the energy cascade from barotropic tides to internal tides, the missing geometrical effects due to unresolved topographic features and basin and shoreline geometry are often unaccounted for. One potential method for improving the quality of the topography and shoreline geometry in the model is to represent the effect of sub-grid scale topography via porous barriers.

In this work, we evaluate the effect of porous barriers, on tides, following the methodology from Adcroft (2013). In essence, porous barriers introduce sub-grid scale topographic information at grid cell walls in finite volume ocean models, which can potentially mitigate the limitation on topography details imposed by model's horizontal resolution. Traditionally, the grid cell walls in finite volume ocean models are fully-opened and uniformly-wide, and the complicated topography features that grid cell walls transect (as depicted in Figure 1a) are therefore ignored. The concept of porous barriers is to model the grid cell walls as permeable barriers in which the openness changes vertically. In practice, we use the statistics of the complicated sub-grid depth profile (D_{shallow}, D_{mean}, and D_{deep} in Figure 1) and approximate with a simplified structure that widens monotonically from the very bottom to the highest point of the topography (e.g., Figure 1b). Effectively, the depth profile reduces the area available for

transport and other fluxes through faces to match the unblocked widths at each depth, which provides a connectivity that matches the real ocean.

With porous barriers, the model has additional degrees of freedom to represent the topography without increasing the model's horizontal resolution and the computational burden that comes with the increased resolution. In Adcroft (2013), an application to a tsunami event showed that the porous barriers can reduce the error of travel times of the surface gravity wave in low-resolution simulations. Here we expand the use of porous barriers to a global implementation and study its application to barotropic tides.

We conduct numerical experiments using Modular Ocean Model version 6 (MOM6; Adcroft et al., 2019) as a barotropic tide model. To better simulate tides, we introduce a new inline self-attraction and loading (SAL) scheme in MOM6. The SAL term accounts for the deformation of the seafloor by the load of the seawater, the gravitational self-attraction of the so-deformed solid earth, and the geoid changes from the gravitational attraction of the seawater itself (Hendershott, 1972; Ray, 1998). The SAL effect applies to all motions of seawater that change mass (bottom pressure) but is especially important for high-frequency motions such as tides. For tides, the SAL term is approximately equal to 10% of the basin-scale tidal SSH signal. The calculation of SAL requires spherical harmonic transforms of global bottom pressure anomaly, which was historically considered too expensive to calculate inline. Other SAL schemes (e.g., scalar approximation, reading in observed SAL fields, and iterative method) have been adopted to circumvent the need for a fully inline SAL calculation, but these approaches are either highly inaccurate or not applicable to non-tidal motions or evolving tides in a changing climate. In recent years, a number of ocean models and earth system ocean component models have begun to compute SAL inline (Barton et al., 2022; Brus et al., 2023; Schindelegger et al., 2018; Shihora et al., 2022; Vinogradova et al., 2015). A similar effort is made in MOM6 and results in this work demonstrate the utility of inline SAL.

The key conclusion from this work is that porous barriers significantly improve barotropic tides. We first use a numerical experiment with 0.04° horizontal resolution as a baseline to evaluate tidal simulation in MOM6. Two sets of numerical experiments with various resolutions, with and without porous barriers, are constructed from the baseline experiment. We found globally implemented porous barriers help reduce the increased tidal errors caused by the coarsened horizontal resolutions.

2. Model Description

We use the Modular Ocean Model version 6 (MOM6; Adcroft et al., 2019) for the numerical experiments. MOM6 uses an Arakawa C-grid for discretization in the horizontal direction. For the experiments in this work, we apply a global tri-polar grid with various numerical resolutions. MOM6 adopts generalized vertical coordinates with vertical Lagrangian remapping (Griffies et al., 2020). In this work, we focus on the barotropic tides and therefore only one layer is used. Layer continuity equation in the model is calculated with volume fluxes using a directionally split piecewise parabolic method (PPM; Colella & Woodward, 1984; Lin et al., 1994). A barotropic-baroclinic split time stepping scheme is used in MOM6 (Hallberg, 1997; Hallberg & Adcroft, 2009). The split time stepping allows for the solution of linearized momentum and continuity equations in the short barotropic time steps, and effectively reduces the time interval of calculating other forcing terms in the momentum equation, including the nonlinear advection, viscosity and SAL terms. Therefore, although split time stepping is designed to relax time step constraints in multi-layer simulations, it also benefits the computational cost of one-layer runs.

MOM6 is capable of simulating wetting and drying, that is, allowing land cells with a "depth" above sea level to be flooded and ocean cell thickness to vanish. Wetting and drying effectively allow the locations of the coastlines to vary over time, which can be potentially important for the tides.

The one-layer configuration of MOM6 is governed by shallow-water equations (see Appendix A). Here we elaborate the momentum terms that are most relevant to barotropic tides. Our simulations are driven by the astronomical forcing of the principal lunar semidiurnal tide M_2, unless otherwise noted. The equilibrium tide η_{EQ} is expressed in Equation 1 (e.g., Arbic et al., 2018).

$$\eta_{EQ}(\lambda, \theta) = (1 + k_2 - h_2) f(t_{\text{ref}}) A \cos^2(\phi) \cos[\omega(t - t_{\text{ref}}) + 2\lambda + \chi(t_{\text{ref}}) + \nu(t_{\text{ref}})] \tag{1}$$

Here, A is the astronomical forcing amplitude and ω is the frequency. k_2 and h_2 are the degree-two Love numbers accounting for the changes in gravitational potential field and seafloor deformations, respectively, associated with

the solid earth body tides (the direct response of the solid earth to the astronomical tidal potential). $\chi(t_{ref})$ is an astronomical argument that is a function of the solar and lunar positions at reference time t_{ref}. $f(t_{ref})$ and $\nu(t_{ref})$ are nodal correction factors to the amplitude and phase, respectively, due to low frequency tidal constituents that are often dropped in tidal simulations and that modulate larger tidal constituents such as M_2. ϕ, and λ are latitude and longitude, respectively. To simplify, we use an idealized calendar at time zero, that is, we set t_{ref} and $\chi(t_{ref})$ to zero, and ignore the nodal correction factors. These simplifications do not affect the conclusions of our work here, as long as the corresponding harmonic analysis is simplified in the same manner.

The energy input from astronomical forcing is balanced by dissipation due to both horizontal and vertical viscous terms. For the horizontal closure, we use a biharmonic form friction with Smagorinsky viscosity (Griffies & Hallberg, 2000). The primary dissipation of barotropic tides is conducted by two types of vertical viscosity. First, a quadratic bottom boundary layer drag, calculated implicitly, is mainly responsible for tidal dissipations in shallow shelf regions where tidal velocities are often as large as 1 m/s. Second, a parameterized linear topographic wave drag is included to represent dissipation by loss to internal tides, a process that is absent in barotropic simulations. We use the wave drag scheme by Jayne and St. Laurent (2001) (see Appendix B for more details). Here, wave drag is calculated implicitly in the barotropic solver as a part of the barotropic momentum equation. The linear wave drag contains a tunable non-dimensional coefficient, used to optimize the global tides. For most simulations in the paper, this coefficient is the only tunable parameter.

For fast-evolving motions such as the tides, the SAL effect must be taken into consideration. The SAL is often calculated via spherical harmonic transforms of the global bottom pressure anomaly, with their spherical harmonic components multiplied by a scaled factor (Equation 2).

$$p_{SAL}(\lambda, \theta) = \sum_{n=0}^{N} \sum_{m=-n}^{n} \frac{3}{\rho_e(2n+1)} \left(1 + k_h - h_h\right) \widetilde{\Delta p_{bot}}^{(n,m)} Y^{(n,m)}(\lambda, \theta) \tag{2}$$

Here, $Y^{(n,m)}$ is the spherical harmonic with degree n and order m. $\widetilde{\Delta p_{bot}}^{(n,m)}$ is the corresponding spherical harmonic component of bottom pressure anomaly. ρ_e is density of solid Earth. k_h and h_h are load Love numbers with degree n, representing seawater load induced changes in gravitational potential field and seafloor deformations, respectively. N is the highest degree used to calculate SAL. For barotropic simulations, bottom pressure anomaly can be reduced to a linear function of SSH anomaly, that is, $\widetilde{\Delta p_{bot}}^{(n,m)} = \rho_0 g \tilde{\eta}^{(n,m)}$ and $p_{SAL} = \rho_0 g \eta_{SAL}$, where g is gravitational acceleration, ρ_0 is average seawater density, $\tilde{\eta}^{(n,m)}$ is degree-n and order-m spherical harmonic component of SSH anomaly, and η_{SAL} is SSH anomaly equivalent of SAL effect.

An inline SAL calculation following Equation 2 is implemented in MOM6 with similar algorithms as in Brus et al. (2023). Following Brus et al. (2023), we use $N = 40$ for barotropic tide experiments. For our baseline 0.04° global barotropic case, inline SAL increased the total computational cost by 20% and, as a fraction of the total, this would be significantly reduced in baroclinic cases that typically have O(50) levels. Inline SAL method leads to the most accurate tides in almost all of our numerical experiments. A comparison of inline SAL and two traditionally used SAL schemes (scalar approximation and read-in method) is discussed in Appendix C.

We run all numerical experiments with a duration of 20 model days, allowing the global barotropic tides to reach equilibrium. We use the SSH from day 18 to 20 for harmonic analysis and compare the results with observations.

3. Methods and Experiment Design

3.1. Model Validation Metrics

We use an observationally-based data-assimilative barotropic tide product TPXO (Egbert & Erofeeva, 2002) version 9 as our reference for tides in the real ocean. For a grid point at (λ, θ) and at given time t, we obtain from harmonic analysis of SSH the M_2 constituent driven sea surface elevation, $h(\lambda, \theta, t) = \text{Re}[A(\lambda, \theta) \exp\{i[\omega t - \phi(\lambda, \theta)]\}]$. Here, A is the amplitude and ϕ is the phase of the tide, respectively. Mean squared errors (MSE), $\epsilon^2(\lambda, \theta)$, of the sea surface elevation h between the model output and TPXO (subscripts m and o, respectively) are calculated as in Equation 3a to quantify the model's deviation from observations. Here, T is the time period of a tidal cycle. Further, the MSE ϵ^2 can be decomposed into contributions from amplitude ϵ_a^2 and phase ϵ_p^2 (Shriver et al., 2012), shown as the two terms in Equation 3b. For the rest of the paper, we show on maps the square-root of MSE, ϵ, and its decompositions ϵ_a and ϵ_p, with the unit of height.

Table 1
List of Experiment Resolutions

Number of grid cells ($nx \times ny$)	Nominal resolution
9000×7056	0.04°
4500×3528	0.08°
3000×2352	0.12°
1500×1176	0.24°
1000×784	0.36°

Note. nx and *ny* refer to the number of grid points in the *x* (nominally zonal) and *y* (nominally meridional) directions.

$$\epsilon^2(\lambda,\theta) = \frac{1}{T}\int_0^T [h_m(\lambda,\theta,t) - h_o(\lambda,\theta,t)]^2 dt \tag{3a}$$

$$= \underbrace{0.5(A_m - A_o)^2}_{\epsilon_a^2(\lambda,\theta)} + \underbrace{A_m A_o\left[1 - \cos(\phi_m - \phi_o)\right]}_{\epsilon_p^2(\lambda,\theta)} \tag{3b}$$

We evaluate the overall performance of each experiment with the root mean square (RMS) of the globally averaged MSE. To reduce potential observation errors from the satellite in coastal and polar regions, we confine the definition of "global average" to within the latitudes 66°S and 66°N and depths larger than 1,000 m (Arbic et al., 2004).

3.2. Baseline Experiments

We start off with a baseline experiment having a nominal horizontal resolution of 0.04° and use it as a benchmark. This baseline experiment serves as the "truth" of the subsequent experiments and presumably has the smallest RMS errors for the M$_2$ tide relative to the rest of the experiments in this work. The only external inputs to the model are topography (see below) and prescribed wave drag piston velocity (see Appendix B).

The topography of the baseline case is generated from the 30-s GEBCO_08 20091120 global data set by taking a 5×5 average at each 0.04° tripolar grid point with the minimum depth set to be above sea level and can therefore be flooded. This is further smoothed with a 2D 1-2-1 smoother except near the coastline (−5 m). Finally, Antarctic ice shelves are "sunk" so that the bathymetry under ice shelves represents the water there. Ice shelves are taken from a 1/2 by 1/4° version of BEDMAP1 (Lythe & Vaughan, 2001). The data sets going into the bathymetry are relatively old because this is a version of the US Navy's GOFS 3.5 (Metzger et al., 2020) bathymetry, although the latter has the coastline at 0.1 m and has additional manual edits in some regions.

We use the 0.04° topography from this run as a source for generating sub-grid scale topography in all subsequent numerical experiments. In other words, coarser resolution experiments do not receive topographic details beyond the topography data set used in the baseline run. In theory, the baseline run should have the highest accuracy of tides.

3.3. Coarsened Horizontal Resolutions

To quantify tidal simulation performance change in lower resolutions, we coarsen the grid of 0.04° simulations by a series of factors. By choosing integer factors, we guarantee that grid cell walls in coarsened resolutions are simply concatenations of grid cell walls in the baseline run, thus simplifying implementation of porous barriers. Resolutions of the numerical experiments vary from 0.04° to 0.36° (Table 1). Along with the grid, the data sets for input topography, wave drag piston velocity is also weighted averaged (by cell area) to serve as inputs for the coarsened resolution simulation.

In the coarsened topography, shoreline configuration, essential for both local and remote tides, is inevitably modified. The locations of the model's discretized coastline depend heavily on the criterion for qualifying a grid cell in the coarsened resolution as an ocean cell. In the simplest scenario, we can arbitrarily choose a cutoff ratio of the ocean area in the coarsened cells ranging from 0 to 1, where 0 results in more ocean cells and therefore more landward retreated coastlines while 1 gives more seaward moving coastlines. Without a better argument to support either the "more ocean" or "more land" coastlines, we use 50% as our cutoff for ocean cells.

Following previous works (Buijsman et al., 2015, 2020; Egbert et al., 2004), the linear wave drag is re-tuned for different horizontal resolutions, as well as different SAL schemes. The globally averaged SSH RMS error is used as the criterion to decide the optimal non-dimensional coefficient for the linear wave drag at each resolution.

3.4. Porous Barriers

3.4.1. Implementation

Effectively, porous barriers constrain transport across the vertical walls of grid cells, thus avoiding the overly-widened pathways between cells. This is achieved by including a non-dimensional factor that approximates

the openness of the grid cell widths used for calculating transport. The discretized continuity equation in the model can be approximated as

$$h^{n+1} = h^n + \frac{\Delta t}{\Delta_x \Delta_y} \cdot \left[\delta_x \left(u \cdot h_x^* \alpha_x \Delta_y \right) + \delta_y \left(v \cdot h_y^* \alpha_y \Delta_x \right) \right] \tag{4}$$

Here, δ_x and δ_y are finite differencing operators x and y direction, respectively. h^n is the layer thickness at time step n. u and v are velocity components in the x and y direction, respectively. h^* is used to stand for the effective thickness at the velocity points from PPM reconstructed volume fluxes. Δ_x and Δ_y are the time-invariant grid cell widths in the x and y direction, respectively. Δt is the time step size. α_x and α_y are the non-dimensional factors from porous barriers for transport at x and y directions, respectively. The α parameters, located at velocity cells (i.e., grid cell walls in C-grid models), are calculated as follows:

$$\alpha = \frac{\int_{\eta_b}^{\eta_t} w(z) dz}{\eta_t - \eta_b} \tag{5}$$

η_t and η_b are the top and bottom interface heights of the layer at the corresponding velocity point. In MOM6, the time-variant layer interface height is calculated at tracer cells (i.e., grid cell centers in C-grid models). For simplicity, η_t and η_b at velocity points are evaluated as the arithmetic mean of the interface heights at the neighboring tracer cells. $w(z)$ is a non-dimensional weight function of depth z, which describes the openness of a grid cell as illustrated in Figure 1b. With $w(z) \leq 1$, α_x, and α_y are guaranteed to be no larger than 1. $w(z)$ is calculated analytically from the approximated depth profiles at the velocity points (the red curve in Figure 1), discussed in details in the next section.

3.4.2. Topography Profiles at Velocity Points

The prescribed local topography vertical profiles are constructed by statistical parameters from high resolution data sets. Following Adcroft (2013), we use three parameters: shallowest, deepest and mean depths at the cell walls, to form a simple idealized V-/U-shape depth profile, which infers sub-grid scale features.

From the baseline topography, we calculate ocean depths at grid cell walls by interpolating from those at the centers of adjacent grid cells. There are multiple choices of interpolation methods, and the best choice is probably specific to the problem being addressed. For instance, for a hydrologically-controlled downward flow in a channel, using the shallowest depth of adjacent cells may better describe the problem. The directions of tidal flow reverse constantly, such that the basin shape and therefore the tidal resonance is perhaps more important. Therefore we use a simple average of the adjacent tracer cell depths here.

We can then generate topography profiles for coarsened resolutions using this 0.04° map of topography at the walls. For each coarsened resolution, the shallowest, deepest and mean depths are obtained from the grid cell walls of the 0.04° resolution that constitute new walls in the new resolution (Figure 2). For instance, at the 0.12° resolution, which is constructed by aggregating 3 × 3 grid cells from the 0.04° configuration, there are three depth values at the grid cell walls at each direction; and the maximum, minimum and mean of these three values are used as parameters to construct the depth profile. Note that by design, the numbers of grid cells of the baseline run in both directions are always multiples of the number in the low-resolution runs, therefore the grid cell walls in the low-resolution always coincide the grid cell walls in the baseline run. It is worth mentioning that the shallowest, deepest and mean depths (i.e., $D_{shallow}$, D_{mean}, and D_{deep} in Figure 1) are determined only by sub-grid scale depth values at grid cell walls, not by cell center depth values. For each coarsened resolution, the depth profiles at the walls are uncorrelated to depths in their nearby tracer cells. The depth profiles are additional degrees of freedom inherited from the baseline topography.

4. Results: Sensitivity to Horizontal Resolutions

4.1. Tides From the Baseline Experiment

We show amplitude and phase of SSH induced by M_2 tides from the baseline experiment in MOM6 (Figure 3a) and compare modeled SSH fields with observations (Figure 3b). The non-dimensional linear wave drag
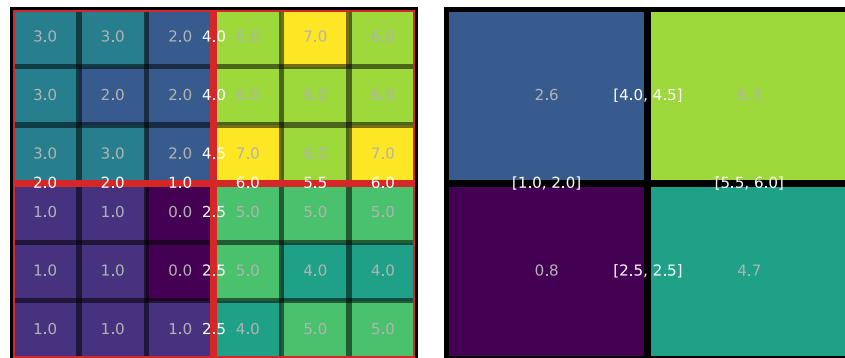
Figure 2. Illustration of the method for generating the depth profiles at grid cell walls. From a high-resolution topography data set (left panel), we can calculate the wall depth with a simple arithmetic mean (numbers in white color) from neighboring cell center depths (numbers in gray color). When horizontal resolution is coarsened (right panel), an area-weight average is used to obtain the new cell center depths, while a range of depths at new walls (numbers in the brackets in white color) is given. The statistics of these depths (e.g., maximum, minimum and mean) can be used to generate a simple-shaped profile. Note that grid cell numbers in the baseline case are always multiples of grid cell numbers in coarsened resolutions, making the new walls in coarse resolutions always concatenations of the old walls in the baseline case.

coefficient is 0.8, which gives the smallest global RMS tidal error. Visually, the spatial distribution of the amplitude and phase match with the real ocean tides. A quantitative comparison between the model and observations is shown in Figure 4a. Overall, the 0.04° resolution MOM6 simulation has an RMS error of 3.74 cm in the deep ocean outside of high latitudes. This is to be compared with previous results such as 5 cm in Egbert et al. (2004), 4.4 cm in Schindelegger et al. (2018), 1.94 cm in Blakely et al. (2022) and 6.8 cm in Barton et al. (2022). The SSH error is mostly dominated by tides in the Atlantic basin, possibly related to the strongly resonant tides in the Hudson Bay (Arbic et al., 2007, 2009). In the Pacific and Indian Oceans, tidal errors are comparatively weaker but are still noticeable near the high tides areas between the amphidromic points.

The total error at each grid point is further decomposed into contributions from amplitude (Figure 4b) and phase (Figure 4c). The large Atlantic errors are mostly attributed to the phase term. For cotidal lines near the counterclockwise amphidromic points in the Atlantic, MOM6 is leading in phase to TPXO. This phase offset, multiplied by large amplitude, results in large phase errors. Similar phase offsets between model and observations can be found in some other places, but the phase error contributions are weak with a low tidal amplitude (see Equation 3b).

Tides are sensitive to locations of coastlines, which undergo constant changes in the real ocean due to flood and ebb tides. Therefore we also test the effect of allowing wetting and drying in the baseline configuration. The global tidal error reduction is about 0.02 cm at the 0.04° resolution. This reduction indicates that while changing coastlines does have an effect on open ocean tides, the resulting effect is much smaller than the effects of porous
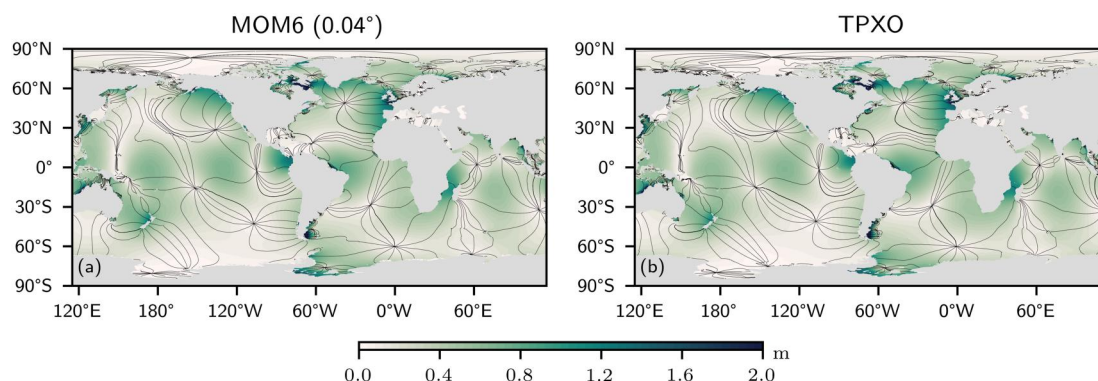

Figure 3. Maps of M_2 surface tide amplitude (colors) and phase (contours) from MOM6 (a) and TPXO atlas (Egbert & Erofeeva, 2002) (b). Phase contours have an interval of 30°. The MOM6 maps are from the baseline experiment, which has a nominal 0.04° horizontal resolution and uses inline SAL.
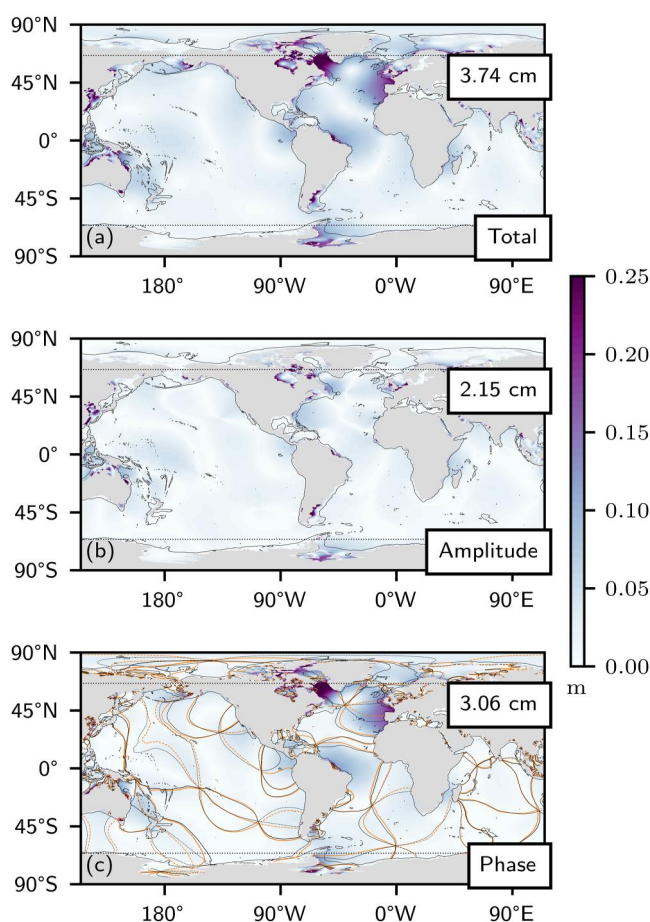
Figure 4. Maps of the square-root of MSE ϵ of SSH between the baseline experiment in MOM6 and TPXO (a) and decomposition into contributions from amplitude ϵ_a (b) and phase ϵ_p (c). Cotidal lines from MOM6 (orange) and TPXO (dark gray) are overlaid in (c) for comparison. Numbers on maps show averaged RMS error over the deep ocean and outside of high latitudes. Contours of 1,000 m depth are shown in light gray curves and the latitudes of 66°N and 66°S are shown in dotted gray lines, which delineate the deep-ocean area over which RMS errors are computed.

barriers that we focus on in this work (as we show in the following). Nonetheless, we adopt wetting and drying in all of our numerical experiments.

4.2. The Effect of Horizontal Resolution

We next investigate how tidal errors change as a function of horizontal resolution. To obtain the smallest RMS error, the linear wave drag is re-tuned for each run with a new resolution. It is found that the non-dimensional coefficient needs to increase at lower resolutions. The averaged RMS errors of tidal SSH from coarsened resolution experiments are shown in Figure 5 (solid curves, the dashed curves are discussed later in Section 5.2). Tidal errors increase almost linearly with decreased horizontal resolution, consistent with results in previous studies (e.g., Egbert et al., 2004).

The decomposition of the total error suggests that the phase error increases faster than the amplitude error as resolution is decreased, such that phase error makes the greater contribution to higher tidal SSH errors at low resolutions. The change in tidal amplitude is directly associated with tidal energetics. Tidal currents are usually weaker with lower resolution horizontal grids, which would change tidal dissipation and energy input. The phase, on the other hand, is also affected by propagations and reflections of the shallow-water gravity waves. When horizontal resolution is coarsened, the model topography also changes. It is likely that the geographic locations of cotidal lines and amphidromic points are changed due to the changes of ocean basin geometries.
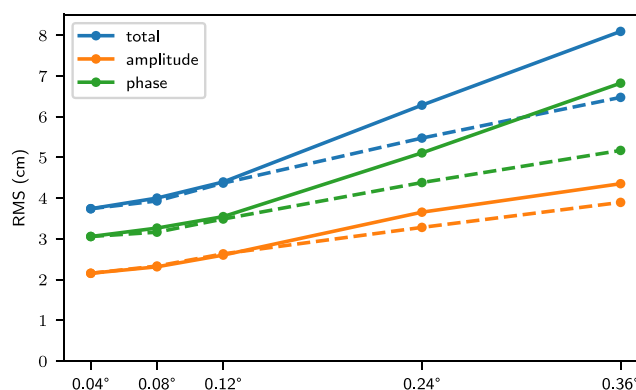
Figure 5. Globally averaged RMS errors for M_2 tides as a function of horizontal resolution. RMS errors are calculated over the deep ocean and outside of high latitudes. The total error (blue) is decomposed into contributions from amplitude (orange) and phase (green). Solid curves show results from control experiments in which topography is simply coarsened (discussed in Section 4.2) and dashed curves show results from the same setup with porous barriers implemented (discussed in Section 5.2).

The spatial distribution of the increased errors in low-resolution runs is exemplified by the 0.36° case in Figure 6. The RMS error increase is not uniform across ocean basins. The greatest differences appear in the Pacific and Indian Oceans, where tidal errors in the baseline case are small. We decompose the total MSE to contributions from each basin in Figure 7. While tidal errors change monotonically across resolutions in almost all ocean basins, the increase in the Pacific, Indian and Southern Oceans are particularly large, especially in the two lowest resolution cases. In particular, the Pacific basin is the primary driver of tidal error increases at low resolutions, largely due to the phase error (Figure 6c).

It is also worth mentioning that there are regions in which the tidal errors decrease at lower resolutions, notably in the region north of New Zealand, and in some parts of the Atlantic basin including Hudson Bay.

5. Results: The Effect of Porous Barriers

5.1. Local Implementation

As discussed in Section 3.4.1, porous barriers effectively narrow grid cells in coarse resolutions. Therefore, if implemented at choke points between a marginal sea and the open ocean, porous barriers will modify the connectivity in that place, potentially changing tides in remote deep oceans. We add porous barriers near the Hudson Strait (Figure 8a) at the coarsest resolution (0.36°). The Hudson Strait connects the Hudson Bay, with high tides and dissipation rates (Cummins et al., 2010; Egbert & Ray, 2000), to the open ocean of the North Atlantic; it has been shown to be one of the key locations where topography can influence both local and remote tides. As shown in Figure 8b, the tidal errors become worse with porous barriers implemented at the mouth of Hudson Strait. The changes in the tidal SSH extends from the Labrador Sea to the entire Atlantic basin, and reach as far as the western Pacific through the Indian Ocean. This result highlights the role that marginal seas play in the deep ocean tides. The response in tidal errors here is rather similar to the findings in Arbic et al. (2009), in which the Hudson Strait is completely blocked in one of their experiments. We speculate the large tidal errors in the Atlantic from the baseline experiment (Figure 4) could be associated with relatively inadequate topography representations near the Hudson Strait; and porous barriers do nothing but reintroduce these inaccurate topographic features to the coarse resolution runs (Note from Figure 6 that the coarse resolution tidal error in fact slight decreases in the Labrador Sea).

The example here demonstrated the model's sensitivity to sub-grid scale topography and the utility of porous barriers to recover some effects from unresolved topographic features. The remote response to local topography modification suggests a global implementation of porous barrier will be far more complicated. The effect of a global implementation may not be a simple summation of all the responses due to the specific local changes, as we show in the next section.
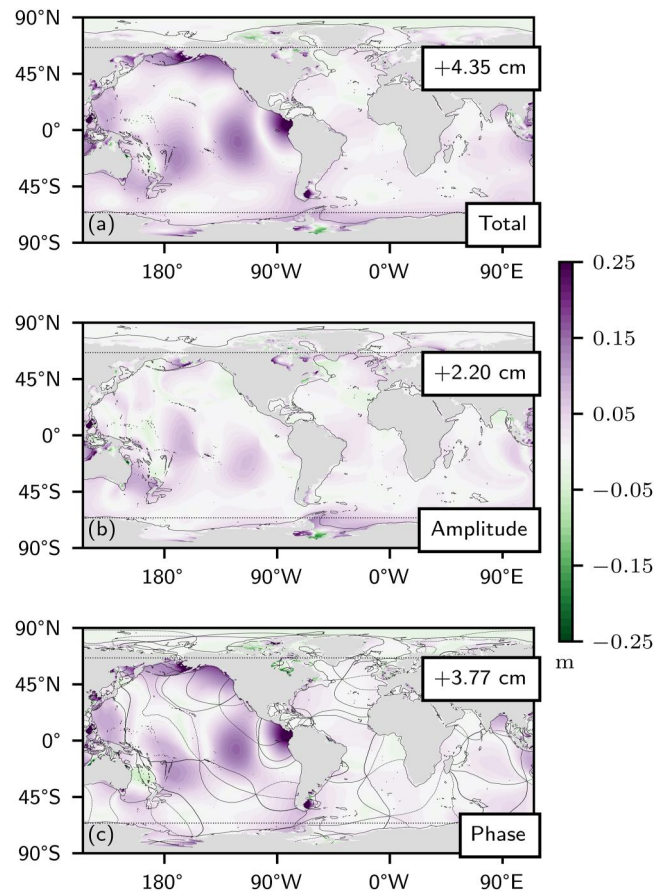
Figure 6. Maps of changes in square-root of MSE ϵ and its amplitude ϵ_a and phase ϵ_p components between 0.36° resolution and the baseline experiment (0.04°). Numbers on maps show changes of globally averaged RMS error. Cotidal lines from the baseline experiment are overlaid in (c) to help locate the changes. Contours of 1,000 m depth are shown in light gray curves and the latitudes of 66°N and 66°S are shown in dotted gray lines, which delineate the deep-ocean area over which RMS errors are computed.
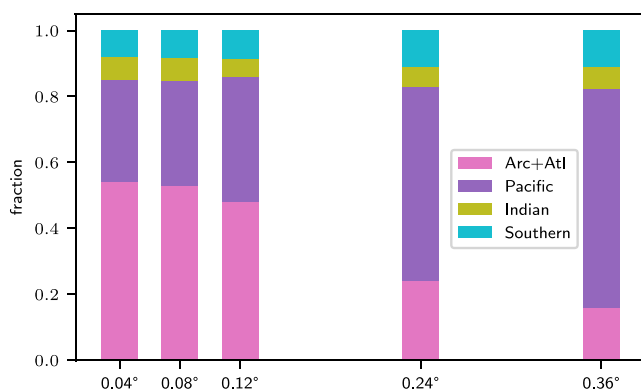
5.2. Global Tidal Error Change

We now evaluate the effect of a global implementation of porous barriers. Porous barriers are added in each coarsened resolution and results are shown in the dashed curves in Figure 5. For each resolution, the only difference in model configuration is the application of porous barriers. Other parameters, for example, the wave drag coefficient, is not re-tuned. Sensitivity to the wave drag coefficient is tested in all porous barrier cases, and we find the optimal wave drag coefficients are identical to the experiments without porous barriers.

In all cases with coarsened horizontal resolution, the total tidal error is decreased with a global implementation of porous barriers. For instance, with the help of porous barriers, the globally averaged RMS error in 0.36° case is comparable with that of the 0.24° case without porous barriers. In most cases, the reduction of tidal error results from reduction in both amplitude and phase errors. Phase error changes are greater than amplitude error changes and are therefore the more dominant factor underlying changes in total errors.

Figure 7. Relative contribution of each ocean basin to the total MSE (without porous barriers) at each resolution. Divided ocean basins: Atlantic and Arctic Oceans (pink), Pacific Ocean (purple), Indian Ocean (olive) and Southern Ocean (cyan).

Geographically, signs and magnitudes of tidal error changes are not uniform. The overall improvement results from large and widespread tidal error
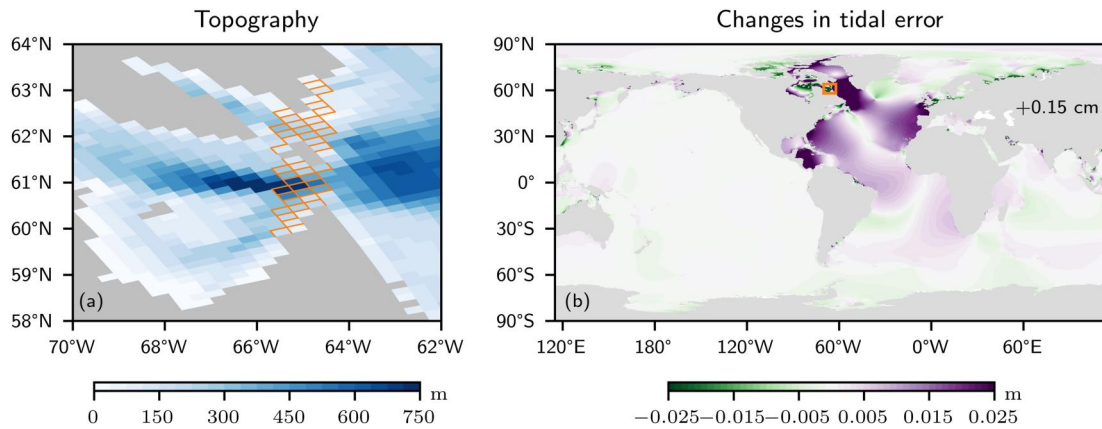
Figure 8. (a) Topography near the mouth of Hudson Strait (shaded color) and grid points where porous barriers are applied (orange lines) at 0.36° resolution. Results are not sensitive to the subtleties of exact locations where porous barriers are added, provided the mouth of the strait is covered. (b) Changes in total tidal error at 0.36° resolution due to local implementation of porous barriers at Hudson Strait. The orange box shows the location of the map in (a).
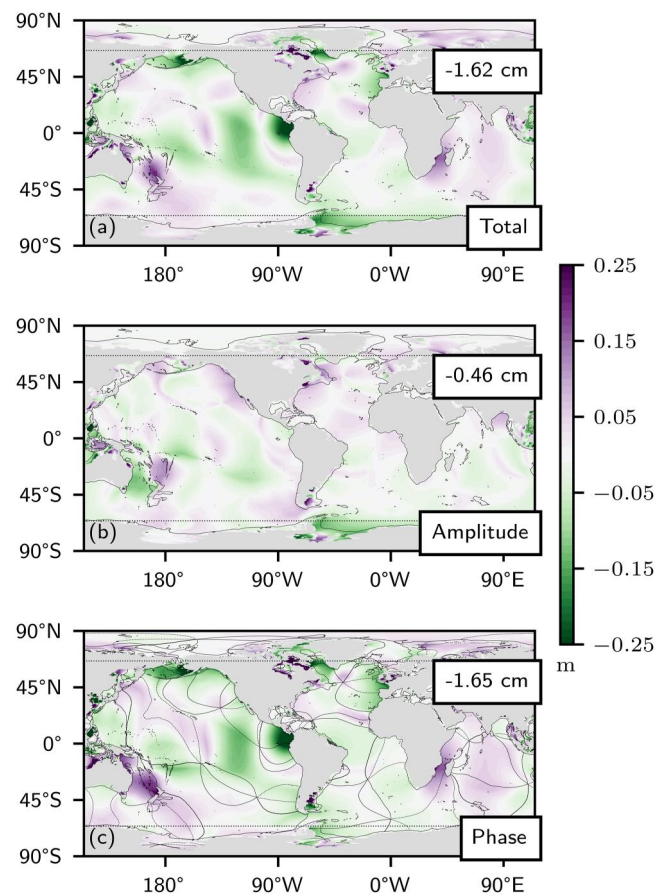

Figure 9. Maps of changes in square-root of MSE ϵ and its amplitude ϵ_a and phase ϵ_p components from the experiment with porous barriers compared with the one without at 0.36° resolution. Numbers on maps show changes of globally averaged RMS error. Contours of 1,000 m depth are shown in light gray curves and the latitudes of 66°N and 66°S are shown in dotted gray lines, which delineate the deep-ocean area over which RMS errors are computed.

Table 2
Changes in Global Tidal Error From 0.36° Resolution (in cm)

Region	Global	Atlantic + Arctic	Pacific	Indian	Southern	No southern
Δε	−1.62	−0.19	−2.78	−0.22	−0.41	−3.03

reductions, but there are also places with increases of tidal error. Generally speaking, most error reductions occur in areas where the tidal error is large compared with the baseline experiment (Figure 9). The globally averaged RMS reduction is largely driven by decreases in the Pacific Ocean, both in the open ocean and along its eastern boundaries. Inversely, tidal error is increased in a number of regions. The southern Indian Ocean and an area north of New Zealand suffer from a significant large tidal error increase. The Atlantic basin overall observes a moderate change, with both signs of change present. Notably, Hudson Bay and western North Atlantic display increases of tidal errors, as with the local implementation in the previous section.

Comparing Figures 6 and 9, it is obvious that porous barriers generally reverse changes arising from coarsening horizontal resolution. It significantly reduces Pacific errors but also brings back some shortcomings in the North Atlantic seen in the baseline run. In other words, porous barriers accomplish what they are intended to accomplish by introducing lost geometric features back to coarse resolutions.

5.3. Possible Optimizations

Even though a local implementation of porous barriers (as in the example of Hudson Strait) may not improve the global tides, the modeled tidal response to a global implementation of porous barriers is favorable. This response suggests there could be possible tuning options to further reduce the total global tidal error. We present here a number of choices based on the configuration of our experiments.

The inhomogeneity of tidal error changes across basins prompts us to examine whether these changes are responses to local or remote implementation of porous barriers. We first explore effects of single-basin implementations of porous barriers. Results from the 0.36° case are listed in Table 2. The global tidal error is reduced for each case where porous barriers are applied to a single ocean. The Pacific-only implementation has the largest effect, even more effective than the global implementation. This suggests that there are cancellations between remote effects of local implementations. In addition, if we exclude the Southern Ocean, the reduction of tidal errors is the greatest, indicating the Southern Ocean's porous barriers have an negative effect on reducing tidal errors.

Inspired by this finding, we further test the dependence of improvement as a function of southern boundaries. We find that 15°S is the optimal southern boundary for implementing porous barriers, and the new configuration drastically reduces tidal errors in coarse resolution simulations (Figure 10). Compared with Figure 5, this optimization leads to further reductions in both phase and amplitude errors, with a greater change in the former.

To further investigate the reason for better tides when porous barriers are not implemented globally, we divide the regions south of 15°S into 20 small domains (Figure 11a), and evaluate their contributions to globally averaged tidal errors. In the first set of experiments, porous barriers are implemented in the target box in addition to the regions north of 15°S. In the second set of experiments, porous barriers are implemented globally but excluding the target box. The results (Figures 11b and 11c) highlight two regions (region around New Zealand, the so-called Zealandia submerged continent, and region around Madagascar), where local porous barriers implementation increases global tidal errors. Tidal error is decreased when porous barriers are implemented excluding either region (and tidal error is increased when either region is included in the north of 15°S configuration). These two regions south of 15°S coincide with the location where tidal errors are increased with global porous barriers (Figure 9), which suggests the local changes in tidal errors are largely due to local porous barriers.
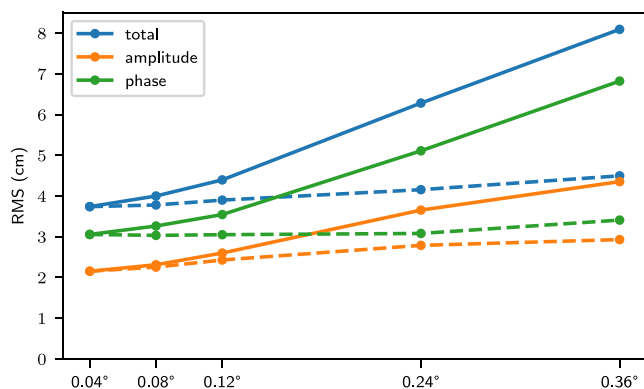

Figure 10. Globally averaged RMS error for M_2 tides as a function of horizontal resolution. As in Figure 5 but for porous barriers implemented only north of 15°S.
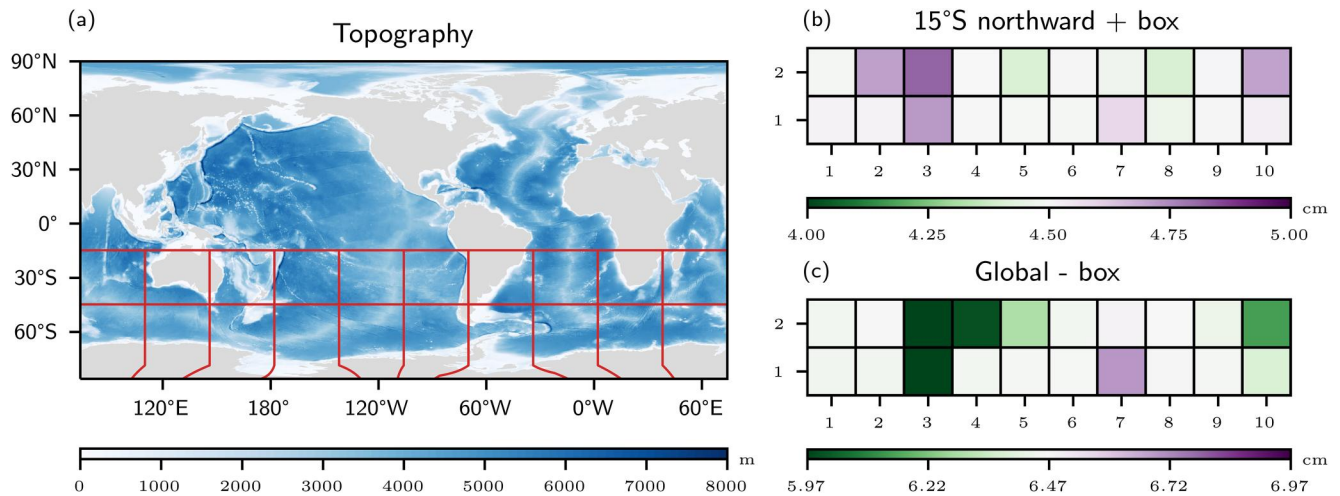
Figure 11. (a) Locations of divided domains south of 15°S for sensitivities of local porous barriers. The domain boxes are shown overlaying on a map of ocean topography. Note that the bended longitudinal lines in the Antarctica are due to the fact that model grid has a dislocated singularity away from the South Pole. (b) Global tidal errors (total errors) from experiments with porous barriers north of 15°S and the corresponding box south of 15°S. (c) Global tidal errors from experiments with global porous barriers excluding the corresponding box south of 15°S. In (b) and (c), the shaded color denotes the changes from the their reference tidal errors, which are 4.50 cm for north of 15°S implementation and 6.47 cm for global implementation, respectively.

These results suggest possibilities of further reducing global tidal errors by tuning the implementation of porous barriers. But more importantly, we further confirm the findings in the previous section, that porous barriers can faithfully reintroduce the sub-grid scale topographic effect to the coarse resolution simulations, which may result in increases of local tidal errors where high-resolution tides are worse than low-resolution.

5.4. Other Tidal Constituents

Sensitivity of tidal errors to porous barriers are tested for non-M_2 tidal constituents, and the global RMS errors are compared in Table 3. Porous barriers are implemented globally for all cases. The results show that porous barriers reduce the global tidal errors for both semidiurnal and diurnal tides.

6. Discussions and Conclusions

In this work, we study the application of porous barriers, a representation of sub-grid scale topography, to global barotropic tides. A series of experiments with various horizontal resolutions are designed. Globally averaged tidal RMS errors, referenced to the observationally-based product TPXO, increase with coarsened resolutions. The error increase is due to contributions from both amplitude and phase, with phase error changes being the relatively larger factor. A global implementation of porous barriers can revert some of the changes from the coarsened horizontal resolution, especially phase errors. Overall, at a given resolution, the globally averaged tidal RMS error is significantly reduced with porous barriers.

Porous barriers are intended to objectively reintroduce sub-grid scale geometric effects from fine resolution topography data sets, which is reflected in tidal error changes of both positive and negative signs. The geographical distribution of tidal error changes from fine to coarse resolution is non-uniform. Specific regions, such as the Hudson Bay, areas around New Zealand, and areas around Madagascar in the southwestern Indian Ocean, exhibit poorer local tides in the baseline experiment with finer horizontal resolution. While in coarsened resolution experiments porous barriers tend to reduce tidal errors in most places, we also observe increases in tidal error in locations that are aligned with regions where tidal errors are larger at finer resolution than coarse resolution experiments.

We explore the possibility of further fine-tuning porous barriers by modifying locations of implementation. Specifically, we target regions where tidal errors are increased with porous barriers. The case with porous barriers

Table 3
Global Tidal Errors of Various Tidal Constituents From 0.36° Resolution (in cm)

	M_2	K_1	S_2	O_1	N_2
$\epsilon_{control}$ (cm)	8.09	2.65	4.07	1.45	1.98
ϵ_{porous} (cm)	6.47	1.91	2.43	1.21	1.45

Note. Only the total errors are shown. For each constituent, the wave drag coefficient is re-tuned to for optimal tides at a given resolution.

implemented only north of 15°S results in even better tidal error reductions than a global implementation. These results are caused by excluding regions with reduced local tidal errors in low-resolution simulations in comparison with the highest resolution case, specifically the two regions south of 15°S. First of all, it is possible that regions where tidal errors are increased by porous barriers are affected by the quality of local and remote topography. Second, the subtleties of Southern Ocean topography may play a role. For instance, simulations in this work do not include dynamical ice shelves in the Antarctica, which has been shown to impact global tidal errors (Pal et al., 2023). Third, the optimal topography configuration may not be necessarily consistent for physical processes of various timescales and frequencies, which means different implementations may be needed depending on the focus of the simulations. For tides, rather than providing conclusive guidelines on how porous barriers should be implemented geographically, we emphasize that this exercise suggests possibilities of further refinement, in which case phase error in particular can be reduced in coarse horizontal resolution simulations.

The objective of this work is to demonstrate the capability of porous barriers and our experiments are designed in an idealized and simple setup. Rather than configuring the most accurate tides in MOM6, we focus on the changes of tidal errors with resolutions and changes with porous barriers at a given resolution. Therefore, instead of extracting sub-grid scale topographic details from finer resolutions, we use topography from a reasonable accurate baseline setup (0.04° resolution) as the source for sub-grid scale topography in coarse resolution runs. This ensures that no further topographic details relative to the baseline are introduced through the application of porous barriers, which allows a self-consistent comparison across model resolutions. In practice, it is likely that the accuracy of the modeled tides can be further improved with finer and more accurate topography than the baseline employed here. We expect porous barriers to be a useful tool to further improve tides with a given source topography data set and horizontal resolution of the model.

The construction and implementation of porous barriers is a rather simplified version compared with Adcroft (2013) in that we are not taking into consideration the structure and connectivity within coarsened grid cells. Adcroft (2013) proposed an objective mapping method to ensure that the effects due to walls within coarsened resolution cells, which would otherwise be ignored, are incorporated into sub-grid scale structure in walls surrounding grid cells, thus avoiding the creation of deep pathways. We choose not to adopt this approach for simplicity. It is possible that with a more faithful construction of porous barriers that includes the inner cell geometries, tides at coarsened resolutions could be further improved. We leave this for possibility as a subject for future research.

Another aspect of sub-grid scale topography is the so-called "porous media," where a profile of topography at cell centers is used to constrain the volume/mass capacity of the grid cells. However, porous media do not affect fully submerged grid cells when there is only one layer in the vertical direction. As discussed in Section 4.1, we did not find the addition of wetting and drying near the coastlines to change our results significantly. Thus we conclude that porous media would not be effective in improving tides in this setup. However, porous medias could potentially be a useful complement to the porous barriers in multi-layer simulations.

Appendix A: Governing Shallow-Water Equations

Dynamics of one-layer barotropic simulations in MOM6 is governed by shallow-water equations (Equation A1 and A2). Here, $\mathbf{u}$ is horizontal velocity, $f + \zeta$ is the total vertical vorticity, where f is the Coriolis parameter and $\zeta = \partial_x v - \partial_y u$ is relative vertical vorticity. η is SSH anomaly of total thickness h referenced to the resting depth of the ocean, η_{EQ} and η_{SAL} are the equilibrium tide and SAL effect, respectively (see Section 2 for their expressions). $\mathbf{F}_{quad}$ is a quadratic bottom drag and $\mathbf{F}_h$ is horizontal viscosity term. $\mathbf{F}_{wave}$ is a parameterized linear wave drag term, elaborated in Appendix B.

$$\partial_t \mathbf{u} = -(f + \zeta)\hat{\mathbf{k}} \times \mathbf{u} - \nabla\left[\frac{1}{2}(u^2 + v^2)\right] - g\nabla(\eta - \eta_{EQ} - \eta_{SAL}) + \mathbf{F}_{quad} + \mathbf{F}_{wave} + \mathbf{F}_h \quad (A1)$$

$$\partial_t \eta = -\nabla \cdot (\mathbf{u}h) \quad (A2)$$

In MOM6, the continuous shallow-water equations above are discretized on an Arakawa C-grid. Porous barriers modify the grid cell widths in the discretized continuity Equation A2, which can be approximated as Equation 5.

Appendix B: Parameterized Linear Wave Drag for Open-Ocean Tidal Dissipation

We adopt the wave drag scheme by Jayne and St. Laurent (2001) (hereinafter, JSL). The adoption of JSL wave drag scheme in this work is similar to Buijsman et al. (2015), to which the readers are referred for more details.

In essence, the wave drag force term is expressed in Equation B1, where χ is a non-dimensional tuning parameter, $\mathbf{u}$ is ocean (barotropic) velocity, and h is total water column thickness. C_{JSL} is a pre-calculated piston velocity that is a function of both bottom roughness and bottom buoyancy frequency. A global map of C_{JSL} for the baseline case (0.04° horizontal resolution) is shown in Figure B1. Note that large C_{JSL} is located near ocean ridges and C_{JSL} is only non-zero for regions deeper than 1,000 m.

$$\mathbf{F}_{\mathrm{wave}} = \chi \frac{C_{\mathrm{JSL}}\mathbf{u}}{h} \tag{B1}$$
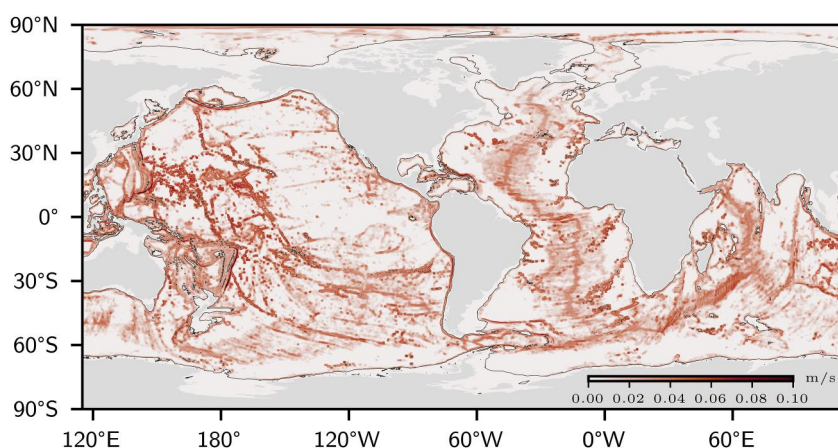

Figure B1. Map of piston velocity C_{JSL} used in Jayne and St. Laurent (2001) linear wave drag scheme. The black contours are used to denote locations of the 1,000-m isobath.

Appendix C: Comparison of Self-Attraction and Loading Schemes

We show a demonstration of the utility of inline SAL in a comparison with two other types of SAL schemes used in previous studies: a scalar approximation (Accad & Pekeris, 1978), in which the SAL is simply a fraction of the SSH anomaly and a read-in method, in which time-invariant amplitudes and phases of the M_2 tidal SAL from observationally-based data set are provided to the models. Inline SAL is more accurate than the scalar approximation because the latter does not account for the scale-selective nature of SAL. In contrast to read-in SAL, inline SAL can be used in studies of past and future tides, in which the tides and their SAL signal have changed significantly. The iterative method, where the ocean model is run repeatedly to get a converged off-line SAL, can also be used for past and future tides, but we exclude it from our tests in this paper because it offers no advantages over inline SAL.

We first compare the results from the baseline simulation in Table C1. For each SAL scheme, wave drag co-efficients are re-tuned and listed in the leftmost column of Table C1. The scalar approximation results in much larger tidal errors than inline SAL. Tidal errors from inline SAL are comparable to these from read-in SAL, which uses observed tidal SAL amplitudes and phases as inputs to the model. Read-in SAL, however, is not applicable to non-periodic motions; moreover, it removes the dynamical feedbacks between bottom pressure anomaly and the SAL term and is therefore incapable of handling the changing tides in climate change scenarios. Due to the obvious advantages in small tidal errors and dynamical justifications, we argue that inline SAL should be the top choice for global tidal simulations.

Next, experiments with coarsened horizontal resolutions and their corresponding experiments with porous barriers are repeated with two other SAL schemes in Figure C1. Consistent with the comparison of the baseline cases, inline SAL results in the most accurate tides for all resolutions (solid curves). The superior performance of inline SAL in lower resolutions over the read-in method suggests the importance of SAL's dynamical interaction. With porous barriers (dashed curves), all SAL schemes show considerable improvement of tidal errors in coarsened resolution simulations, which provides supports to the robustness of results on the utility of porous barriers.

Table C1
Comparison of Three SAL Schemes in the Baseline Case (0.04° Horizontal Resolution)

SAL scheme	Wave drag coefficient	Total (cm)	Amplitude (cm)	Phase (cm)
Inline	0.8	3.74	2.15	3.06
Scalar	1.0	5.98	3.35	4.95
Read-in	0.9	3.81	2.77	2.62

Note. The first column compares wave drag coefficients with the smallest deep-ocean tidal errors. The second columns compares total deep-ocean tidal errors and the last two columns show decompositions of the errors into amplitude and phase.
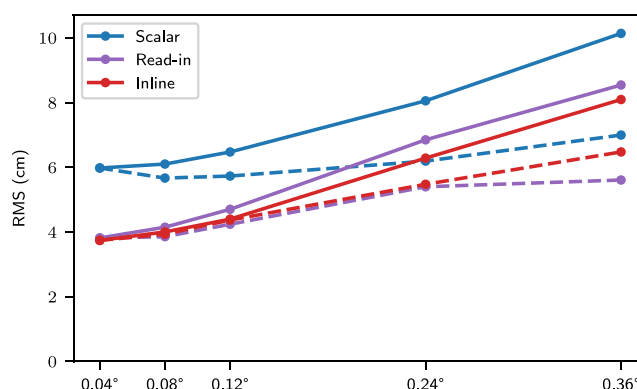
Figure C1. Globally averaged total RMS error for M_2 tides as a function of horizontal resolution for different SAL options. Solid curves show results from control experiments in which topography is simply coarsened and dashed curves show results from the same setup with porous barriers implemented.

Data Availability Statement

The version of MOM6 source code used in all simulations of this work can be found at https://github.com/herrwang0/MOM6/releases/tag/paper_porousbarriers. Runtime parameters, input files for the model, and output from all simulations in this work is stored at Wang et al. (2023) (https://doi.org/10.5281/zenodo.8166251).

References

Accad, Y., & Pekeris, C. L. (1978). Solution of the tidal equations for the M_2 and S_2 tides in the world oceans from a knowledge of the tidal potential alone. *Philosophical Transactions of the Royal Society of London - Series A: Mathematical and Physical Sciences*, *290*(1368), 235–266.

Adcroft, A. (2013). Representation of topography by porous barriers and objective interpolation of topographic data. *Ocean Modelling*, *67*, 13–27. https://doi.org/10.1016/j.ocemod.2013.03.002

Adcroft, A., Anderson, W., Balaji, V., Blanton, C., Bushuk, M., Dufour, C. O., et al. (2019). The GFDL global ocean and sea ice model OM4.0: Model description and simulation features. *Journal of Advances in Modeling Earth Systems*, *11*(10), 3167–3211. https://doi.org/10.1029/2019ms001726

Arbic, B. K. (2022). Incorporating tides and internal gravity waves within global ocean general circulation models: A review. *Progress in Oceanography*, *206*, 102824. https://doi.org/10.1016/j.pocean.2022.102824

Arbic, B. K., Alford, M. H., Ansong, J. K., Buijsman, M. C., Ciotti, R. B., Farrar, J. T., et al. (2018). Primer on global internal tide and internal gravity wave continuum modeling in HYCOM and MITgcm. *New frontiers in operational oceanography*, 307–392.

Arbic, B. K., Garner, S. T., Hallberg, R. W., & Simmons, H. L. (2004). The accuracy of surface elevations in forward global barotropic and baroclinic tide models. *Deep Sea Research Part II: Topical Studies in Oceanography*, *51*(25–26), 3069–3101. https://doi.org/10.1016/j.dsr2.2004.09.014

Arbic, B. K., & Garrett, C. (2010). A coupled oscillator model of shelf and ocean tides. *Continental Shelf Research*, *30*(6), 564–574. https://doi.org/10.1016/j.csr.2009.07.008

Arbic, B. K., Karsten, R. H., & Garrett, C. (2009). On tidal resonance in the global ocean and the back-effect of coastal tides upon open-ocean tides. *Atmosphere-Ocean*, *47*(4), 239–266. https://doi.org/10.3137/oc311.2009

Arbic, B. K., St-Laurent, P., Sutherland, G., & Garrett, C. (2007). On the resonance and influence of the tides in Ungava Bay and Hudson Strait. *Geophysical Research Letters*, *34*(17), L17606. https://doi.org/10.1029/2007gl030845

Arbic, B. K., Wallcraft, A. J., & Metzger, E. J. (2010). Concurrent simulation of the eddying general circulation and tides in a global ocean model. *Ocean Modelling*, *32*(3–4), 175–187. https://doi.org/10.1016/j.ocemod.2010.01.007

Barton, K. N., Pal, N., Brus, S. R., Petersen, M. R., Arbic, B. K., Engwirda, D., et al. (2022). Global barotropic tide modeling using inline self-attraction and loading in MPAS-Ocean. *Journal of Advances in Modeling Earth Systems*, *14*(11), e2022MS003207. https://doi.org/10.1029/2022ms003207

Blakely, C. P., Ling, G., Pringle, W. J., Contreras, M. T., Wirasaet, D., Westerink, J. J., et al. (2022). Dissipation and bathymetric sensitivities in an unstructured mesh global tidal model. *Journal of Geophysical Research: Oceans*, *127*(5), e2021JC018178. https://doi.org/10.1029/2021jc018178

Brus, S. R., Barton, K. N., Pal, N., Roberts, A. F., Engwirda, D., Petersen, M. R., et al. (2023). Scalable self attraction and loading calculations for unstructured ocean tide models. *Ocean Modelling*, *182*, 102160. https://doi.org/10.1016/j.ocemod.2023.102160

Buijsman, M. C., Arbic, B. K., Green, J., Helber, R. W., Richman, J. G., Shriver, J. F., et al. (2015). Optimizing internal wave drag in a forward barotropic model with semidiurnal tides. *Ocean Modelling*, *85*, 42–55. https://doi.org/10.1016/j.ocemod.2014.11.003

Buijsman, M. C., Stephenson, G. R., Ansong, J. K., Arbic, B. K., Green, J. M., Richman, J. G., et al. (2020). On the interplay between horizontal resolution and wave drag and their effect on tidal baroclinic mode waves in realistic global ocean simulations. *Ocean Modelling*, *152*, 101656. https://doi.org/10.1016/j.ocemod.2020.101656

Clarke, A. J. (1991). The dynamics of barotropic tides over the continental shelf and slope. In B. B. Parker (Ed.), *Tidal hydrodynamics* (pp. 79–108). John Wiley and Sons.

Colella, P., & Woodward, P. R. (1984). The piecewise parabolic method (PPM) for gas-dynamical simulations. *Journal of Computational Physics*, *54*(1), 174–201. https://doi.org/10.1016/0021-9991(84)90143-8

Cummins, P. F., Karsten, R. H., & Arbic, B. K. (2010). The semi-diurnal tide in Hudson Strait as a resonant channel oscillation. *Atmosphere-Ocean*, *48*(3), 163–176. https://doi.org/10.3137/oc307.2010

Egbert, G. D., & Erofeeva, S. Y. (2002). Efficient inverse modeling of barotropic ocean tides. *Journal of Atmospheric and Oceanic Technology*, *19*(2), 183–204. https://doi.org/10.1175/1520-0426(2002)019<0183:eimobo>2.0.co;2

Egbert, G. D., & Ray, R. D. (2000). Significant dissipation of tidal energy in the deep ocean inferred from satellite altimeter data. *Nature*, *405*(6788), 775–778. https://doi.org/10.1038/35015531

Egbert, G. D., & Ray, R. D. (2001). Estimates of M_2 tidal energy dissipation from TOPEX/Poseidon altimeter data. *Journal of Geophysical Research*, *106*(C10), 22475–22502. https://doi.org/10.1029/2000jc000699

Egbert, G. D., Ray, R. D., & Bills, B. G. (2004). Numerical modeling of the global semidiurnal tide in the present day and in the last glacial maximum. *Journal of Geophysical Research*, *109*(C3), C03003. https://doi.org/10.1029/2003jc001973

Garrett, C. (1972). Tidal resonance in the Bay of Fundy and Gulf of Maine. *Nature*, *238*(5365), 441–443. https://doi.org/10.1038/238441a0

Griffies, S. M., Adcroft, A., & Hallberg, R. W. (2020). A primer on the vertical Lagrangian-remap method in ocean models based on finite volume generalized vertical coordinates. *Journal of Advances in Modeling Earth Systems*, *12*(10), e2019MS001954. https://doi.org/10.1029/2019ms001954

Griffies, S. M., & Hallberg, R. W. (2000). Biharmonic friction with a Smagorinsky-like viscosity for use in large-scale eddy-permitting ocean models. *Monthly Weather Review*, *128*(8), 2935–2946. https://doi.org/10.1175/1520-0493(2000)128<2935:bfwasl>2.0.co;2

Hallberg, R. (1997). Stable split time stepping schemes for large-scale ocean modeling. *Journal of Computational Physics*, *135*(1), 54–65. https://doi.org/10.1006/jcph.1997.5734

Hallberg, R., & Adcroft, A. (2009). Reconciling estimates of the free surface height in Lagrangian vertical coordinate ocean models with mode-split time stepping. *Ocean Modelling*, *29*(1), 15–26. https://doi.org/10.1016/j.ocemod.2009.02.008

Heath, R. (1981). Estimates of the resonant period and Q in the semi-diurnal tidal band in the north atlantic and pacific oceans. *Deep-Sea Research, Part A: Oceanographic Research Papers*, *28*(5), 481–493. https://doi.org/10.1016/0198-0149(81)90139-4

Hendershott, M. (1972). The effects of solid earth deformation on global ocean tides. *Geophysical Journal International*, *29*(4), 389–402. https://doi.org/10.1111/j.1365-246x.1972.tb06167.x

Jayne, S. R., & St. Laurent, L. C. (2001). Parameterizing tidal dissipation over rough topography. *Geophysical Research Letters*, *28*(5), 811–814. https://doi.org/10.1029/2000gl012044

Lin, S.-J., Chao, W. C., Sud, Y., & Walker, G. (1994). A class of the van leer-type transport schemes and its application to the moisture transport in a general circulation model. *Monthly Weather Review*, *122*(7), 1575–1593. https://doi.org/10.1175/1520-0493(1994)122<1575:acotvl>2.0.co;2

Lythe, M. B., & Vaughan, D. G. (2001). BEDMAP: A new ice thickness and subglacial topographic model of Antarctica. *Journal of Geophysical Research*, *106*(B6), 11335–11351. https://doi.org/10.1029/2000jb900449

Metzger, E., Hogan, P., Shriver, J., Thoppil, P., Douglass, E., Yu, Z., et al. (2020). *Validation test report for the global ocean forecast system 3.5-1/25 degree HYCOM/CICE with tides (Tech. Rep.).* Navel Research Laboratory, Washington DC, United States.

Müller, M. (2007). The free oscillations of the world ocean in the period range 8 to 165 hours including the full loading effect. *Geophysical Research Letters*, *34*(5), L05606. https://doi.org/10.1029/2006gl028870

Müller, M., Haak, H., Jungclaus, J. H., Sündermann, J., & Thomas, M. (2010). The effect of ocean tides on a climate model simulation. *Ocean Modelling*, *35*(4), 304–313. https://doi.org/10.1016/j.ocemod.2010.09.001

Pal, N., Barton, K. N., Petersen, M. R., Brus, S. R., Engwirda, D., Arbic, B. K., et al. (2023). Barotropic tides in MPAS-ocean (E3SM V2): Impact of ice shelf cavities. *Geoscientific Model Development*, *16*(4), 1297–1314. https://doi.org/10.5194/gmd-16-1297-2023

Platzman, G. W., Curtis, G. A., Hansen, K. S., & Slater, R. D. (1981). Normal modes of the world ocean. Part II: Description of modes in the period range 8 to 80 hours. *Journal of Physical Oceanography*, *11*(5), 579–603. https://doi.org/10.1175/1520-0485(1981)011<0579:nmotwo>2.0.co;2

Ray, R. (1998). Ocean self-attraction and loading in numerical tidal models. *Marine Geodesy*, *21*(3), 181–192. https://doi.org/10.1080/01490419809388134

Schiller, A., & Fiedler, R. (2007). Explicit tidal forcing in an ocean general circulation model. *Geophysical Research Letters*, *34*(3), L03611. https://doi.org/10.1029/2006gl028363

Schindelegger, M., Green, J., Wilmes, S.-B., & Haigh, I. D. (2018). Can we model the effect of observed sea level rise on tides? *Journal of Geophysical Research: Oceans*, *123*(7), 4593–4609. https://doi.org/10.1029/2018jc013959

Shihora, L., Sulzbach, R., Dobslaw, H., & Thomas, M. (2022). Self-attraction and loading feedback on ocean dynamics in both shallow water equations and primitive equations. *Ocean Modelling*, *169*, 101914. https://doi.org/10.1016/j.ocemod.2021.101914

Shriver, J., Arbic, B. K., Richman, J., Ray, R., Metzger, E., Wallcraft, A., & Timko, P. (2012). An evaluation of the barotropic and internal tides in a high-resolution global ocean circulation model. *Journal of Geophysical Research*, *117*(C10), C10024. https://doi.org/10.1029/2012jc008170

Thomas, M., Sündermann, J., & Maier-Reimer, E. (2001). Consideration of ocean tides in an OGCM and impacts on subseasonal to decadal polar motion excitation. *Geophysical Research Letters*, *28*(12), 2457–2460. https://doi.org/10.1029/2000gl012234

Vinogradova, N. T., Ponte, R. M., Quinn, K. J., Tamisiea, M. E., Campin, J.-M., & Davis, J. L. (2015). Dynamic adjustment of the ocean circulation to self-attraction and loading effects. *Journal of Physical Oceanography*, *45*(3), 678–689. https://doi.org/10.1175/jpo-d-14-0150.1

Wang, H., Hallberg, R. W., Wallcraft, A. J., Arbic, B. K., & Chassignet, E. P. (2023). MOM6 M_2 tides with porous barriers [Dataset]. *Zenodo*. https://doi.org/10.5281/zenodo.8166251

Wunsch, C. (1972). Bermuda sea level in relation to tides, weather, and baroclinic fluctuations. *Reviews of Geophysics*, *10*(1), 1–49. https://doi.org/10.1029/rg010i001p00001